arXiv:1211.0378v1 [cond-mat.mtrl-sci] 2 Nov 2012

Electronic, mechanical, and thermodynamic properties of americium dioxide

Yong Lu,[1] Yu Yang,[1] Fawei Zheng,[1] Bao-Tian Wang,[1] and Ping Zhang[1,2,*]

[1]*LCP, Institute of Applied Physics and Computational Mathematics, Beijing 100088, China*

[2]*Center for Applied Physics and Technology, Peking University, Beijing 100871, China*

Abstract

By performing density functional theory (DFT) $+U$ calculations, we systematically study the electronic, mechanical, tensile, and thermodynamic properties of AmO_2. The experimentally observed antiferromagnetic insulating feature [J. Chem. Phys. 63, 3174 (1975)] is successfully reproduced. It is found that the chemical bonding character in AmO_2 is similar to that in PuO_2, with smaller charge transfer and stronger covalent interactions between americium and oxygen atoms. The valence band maximum and conduction band minimum are contributed by $2p$-$5f$ hybridized and $5f$ electronic states respectively. The elastic constants and various moduli are calculated, which show that AmO_2 is less stable against shear forces than PuO_2. The stress-strain relationship of AmO_2 is examined along the three low-index directions by employing the first-principles computational tensile test method. It is found that similar to PuO_2, the [100] and [111] directions are the strongest and weakest tensile directions, respectively, but the theoretical tensile strengths of AmO_2 are smaller than those of PuO_2. The phonon dispersion curves of AmO_2 are calculated and the heat capacities as well as lattice expansion curve are subsequently determined. The lattice thermal conductance of AmO_2 is further evaluated and compared with attainable experiments. Our present work integrally reveals various physical properties of AmO_2 and can be referenced for technological applications of AmO_2 based materials.

PACS numbers: 71.20.-b, 62.20.-x, 63.20.D-, 65.40.-b

*Author to whom correspondence should be addressed. E-mail: zhang_ping@iapcm.ac.cn

I. INTRODUCTION

Actinide based materials possess interesting physical behaviors due to the existence of $5f$ electrons and have attracted extensive attentions [1–7], among which the actinide dioxides (AnO_2) have been investigated most widely. At their ground state, all actinide dioxides crystallize in face-centered-cubic (CaF_2-like) structure. In this arrangement, each actinide atom, located at the center of an oxygen cube, is expected in the ionic limit to yield four of its electrons to the surrounding oxygen atoms. This would lead to formal integer $5f$ orbital populations ranging from f^0 (Th) to f^{10} (Fm). Among the dioxide series, PuO_2 and AmO_2 occupy the intermediate zone, before PuO_2 ($ThO_2 \rightarrow NpO_2$) the $5f$ electronic states appear as localized states above the oxygen-$2p$ states, while after AmO_2 ($CmO_2 \rightarrow FmO_2$) the $5f$ electronic states appear as localized states below the oxygen-$2p$ states. Thus the actinide $5f$ electronic states in AmO_2 as well as in PuO_2 have the largest overlap with oxygen-$2p$ states. However, different from the widespread researches on PuO_2 [7–12], AmO_2 have received very few theoretical concerns until now. Therefore following our previous systematic investigations on the ground-state properties and high-pressure behaviors of PuO_2 [11], here we further investigate the corresponding physical properties of AmO_2.

Another reason for a thorough study of AmO_2 is its important role played in the latest nuclear reactor fuels. During the burning cycle of UO_2 in conventional fission nuclear reactors, some considerable amounts of plutonium and neptunium isotopes, as well as smaller quantities of minor actinides such as Am, Cm, Bk, and Cf, emerge in the reaction waste [13]. Since such radioactive waste results in very troublesome long-term storage requirements, it is then suggested that the produced transuranium element dioxides could be reprocessed from the burnt fuel and used as alternative fuel in a new generation of reactors [14–17]. Therefore, the mechanical and thermodynamic properties of these dioxides also need to be investigated and presented. Similar to our previous theoretical studies on PuO_2 [8, 11] and NpO_2 [18], here we will systematically obtain various physical properties of AmO_2 and compare them with attainable experiments as well as possible.

Different physical properties of AmO_2 have been investigated in experiments ever since 1969 [19, 20]. The earlier magnetic susceptibility measurements reveal that AmO_2 undergoes antiferromagnetic transition at 8.5 ± 0.5 K [20]. Recently, along with the development of computing abilities and numerical methods for applying quantum mechanics calculations,

more and more theoretical researches are now being carried out on multi-phase properties of different actinide dioxides. Although problems still exist like on the ground-state magnetic orders [21–25], many theoretically obtained physical properties of dioxides like UO_2 and PuO_2 already accord very well with experiments. For example, the optical spectrum of UO_2 given by employing the density functional theory (DFT) $+U$ method [26] is well consistent with the optical reflectance measurement [27], which has inspired experimentalist [28] to choose the DFT+U results of PuO_2 [26] as a criteria in determining the melting temperature of this material. Also remarkably, the DFT+U predicted phonon spectrum of PuO_2 [11] has been confirmed by the most recent experimental report [29]. Based on these previous successes, in the present paper we intend to reveal the ground-state properties for AmO_2, including electronic, mechanical, and thermodynamic aspects, as well as its high-pressure behaviors.

II. COMPUTATION METHODS

Our DFT calculations are carried out using the Vienna *ab initio* simulations package (VASP) [30] with the projected-augmented-wave (PAW) potential methods [31]. The exchange and correlation effects are described by local density approximation (LDA) and generalized gradient approximation (GGA) in the Perdew-Burke-Ernzerhof (PBE) form [32]. The plane-wave basis set is limited by an energy cutoff of 500 eV. Integrations over the Brillouin Zone of the cubic cell containing 4 americium and 8 oxygen atoms are done on a $9\times9\times9$ k points mesh generated by the Monkhorst-Pack [33] method, which is sufficient for an energy convergence of less than 1.0×10^{-4} eV per atom. The strong on-site Coulomb repulsion among the localized americium $5f$ electrons is described by the DFT+U formalism formulated by Dudarev *et al.* [34–36]. In this method, only the difference between the spherically averaged screened Coulomb energy U and the exchange energy J is significant for the total LDA/GGA energy functional. And in this paper, the Coulomb U is treated as a variable, while the exchange energy is set to be a constant J=0.75 eV. Since only the difference between U and J is significant, thus, we will henceforth label them as one single parameter, labeled as U for simplicity, while keeping in mind that the nonzero J has been used during calculations.

In order to calculate the elastic constants for AmO_2, we enforced small strains on the

equilibrium cubic cell. For small strain ϵ, Hooke's law is valid and the crystal energy $E(V,\epsilon)$ can be expanded as a Taylor series [37],

$$E(V,\epsilon) = E(V_0,0) + V_0 \sum_{i=1}^{6} \sigma_i e_i + \frac{V_0}{2} \sum_{i=1}^{6} \sum_{j=1}^{6} C_{ij} e_i e_j + O(\{e_i^3\}), \tag{1}$$

where $E(V_0,0)$ is the total energy at the equilibrium volume V_0 of the cell without strains, C_{ij} are the elastic constants, and ϵ is the strain tensor which has matrix elements ε_{ij} (i,j=1, 2, and 3) defined as

$$\varepsilon_{ij} = \begin{pmatrix} e_1 & \frac{1}{2}e_6 & \frac{1}{2}e_5 \\ \frac{1}{2}e_6 & e_2 & \frac{1}{2}e_4 \\ \frac{1}{2}e_5 & \frac{1}{2}e_4 & e_3 \end{pmatrix} \quad \begin{matrix} \frac{1}{2}e_6 & \frac{1}{2}e_5 \\ \frac{1}{2}e_4 & \frac{1}{2}e_5 \\ e_3 & \frac{1}{2}e_4 \\ & e_3 \end{matrix} \Bigg). \tag{2}$$

Note that we have used the Voigt notation in the equation above which replaces xx, yy, zz, yz, xz, and xy by 1, 2, 3, 4, 5, and 6, respectively. For cubic structure, there are only three independent elastic constants, C_{11}, C_{12}, and C_{44}. So, we can employ three different strains to calculate them as follows, ϵ^1=(δ,δ,0,0,0,0), ϵ^2=(δ,$-\delta$,0,0,0,0), ϵ^3=(0,0,0,δ,δ,0). The strain amplitude δ is varied in steps of 0.02 from -0.06 to 0.06 and the total energies $E(V,\delta)$ at these strain steps are calculated.

For semiconductors, the Helmholtz free energy F can be expressed as

$$F(V,T) = E(V) + F_{vib}(V,T), \tag{3}$$

where $E(V)$ stands for the ground-state electronic energy, and $F_{vib}(V,T)$ is the phonon free energy at a given unit cell volume V. Under quasi-hamonic approximation (QHA), $F_{vib}(V,T)$ can be evaluated by

$$F_{vib}(V,T) = k_B T \sum_{j,\mathbf{q}} \ln \left[2 \sinh \left(\frac{\hbar \omega_j(\mathbf{q},V)}{2 k_B T} \right) \right], \tag{4}$$

where $\omega_j(\mathbf{q},V)$ is the phonon frequency of the jth phonon mode with wave vector $\mathbf{q}$ at fixed V, and k_B is the Boltzmann constant. The total specific heat of the crystal is the sum of all

phonon modes over the Brillouin zone (BZ),

$$C_v(T) = \sum_{j,\mathbf{q}} c_{v,j}(\mathbf{q}, T). \tag{5}$$

$c_{v,j}(\mathbf{q}, T)$ is the mode contribution to the specific heat defined as

$$c_{v,j}(\mathbf{q}, T) = k_B \sum_{j,\mathbf{q}} \left(\frac{\hbar\omega_j(\mathbf{q}, V)}{2k_B T} \right)^2 \frac{1}{\sinh^2[\hbar\omega_j(\mathbf{q}, V)/2k_B T]}. \tag{6}$$

The mode Grüneisen parameter $\gamma_j(\mathbf{q})$ describing the phonon frequency shift with respect to the volume can be calculated by

$$\gamma_j(\mathbf{q}) = -\frac{d[\ln \omega_j(\mathbf{q}, V)]}{d[\ln V]}. \tag{7}$$

The lattice thermal conductivity κ for a material can be written as a sum over one longitudinal (κ_{LA}) and two transverse (κ_{TA} and $\kappa_{TA'}$) acoustic phonon branches [38, 39],

$$\kappa = \kappa_{LA} + \kappa_{TA} + \kappa_{TA'}. \tag{8}$$

These partial thermal conductivities can be calculated differently, depending on the specific mechanisms for phonon scattering rates $1/\tau_c$, where τ_c is the relaxation time. At relative high temperatures, the dominant mechanism for phonon scattering is the normal and Umklapp phonon-phonon processes ($1/\tau_c = 1/\tau_N + 1/\tau_U$), in which mainly the acoustic phonon branches interact with each other and transport heat. Using the Debye-Callaway model [38, 40], the partial conductivities κ_i (i corresponds to TA, TA′, or LA modes) can be expressed as

$$\kappa_i = \frac{1}{3} C_i T^3 \left\{ \int_0^{\Theta_i/T} \frac{\tau_c^i(x) x^4 e^x}{(e^x - 1)^2} dx + \frac{\left[\int_0^{\Theta_i/T} \frac{\tau_c^i(x) x^4 e^x}{\tau_N^i (e^x - 1)^2} dx \right]^2}{\int_0^{\Theta_i/T} \frac{\tau_c^i(x) x^4 e^x}{\tau_N^i \tau_U^i (e^x - 1)^2} dx} \right\}, \tag{9}$$

where Θ_i is the longitudinal (transverse) Debye temperature, $x = \hbar\omega/k_B T$, and $C_i = k_B^4/2\pi^2\hbar^3 v_i$. Here, $\hbar$ is the Plank constant, k_B is the Boltzmann constant, ω is the phonon frequency, and v_i is the longitudinal or transverse acoustic phonon velocity. The normal phonon scattering and Umklapp phonon-phonon scattering are written as

$$\frac{1}{\tau_N^{LA}(x)} = \frac{k_B^3 \gamma_{LA}^2 V}{M\hbar^2 v_{LA}^5} \left(\frac{k_B}{\hbar} \right)^2 x^2 T^5, \tag{10}$$

$$\frac{1}{\tau_N^{TA/TA'}(x)} = \frac{k_B^4 \gamma_{TA/TA'}^2 V}{M\hbar^3 v_{TA/TA'}^5} \frac{k_B}{\hbar} x T^5, \tag{11}$$

TABLE I: Calculated lattice parameters (a_0), bulk modulus (B_0), pressure derivative of bulk modulus (B_0'), spin moment of each americium ion (μ_{mag}), and energy band gap (E_g) for antiferromagnetic AmO_2 by different calculational methods. Other experimental and theoretical results are also included for comparisons.

Method	a_0 (Å)	B_0 (GPa)	B_0'	μ_{mag} (μ_B)	E_g (eV)
LDA+U (U=0)	5.280	217.7	4.53	4.56	0
LDA+U (U=4)	5.351	189.6	4.71	4.94	0.7
GGA+U (U=0)	5.401	179.3	4.10	4.77	0
GGA+U (U=4)	5.484	140.1	4.81	5.15	1.0
Expt.	5.383[a],5.375[b]				
HSE	5.37[c]			5.1[c]	1.6[c]

[a] Reference 42.

[b] Reference 43.

[c] Reference 7.

and

$$\frac{1}{\tau_U^i(x)} = \frac{\hbar\gamma^2}{Mv_i^2\Theta_i}\left(\frac{k_B}{\hbar}\right)^2 x^2T^3e^{-\Theta_i/3T}, \tag{12}$$

respectively, where γ is the Grüneisen parameter, V is the volume per atom, and M is the average mass of an atom in the crystal. With reasonable expressions of the Debye temperature and acoustic Grüneisen parameter to describe the harmonic phonon branches and the anharmonic interactions between different phonon branches, Eq. (9) can provide reasonable predictions for a material's thermal conductivity.

III. RESULTS AND DISCUSSIONS

A. Structural and electronic properties

Firstly, the equilibrium lattice parameter of AmO_2 is determined from total-energy calculations by the DFT+U methods. The total energies are calculated in a wide range of

lattice constants and fitted to the Brich-Murnaghan equation of states (EOS) [41],

$$E(V) = E_0 + \frac{9V_0B_0}{16}\left\{\left[\left(\frac{V_0}{V}\right)^{2/3} - 1\right]^3 B_0' + \left[\left(\frac{V_0}{V}\right)^{2/3} - 1\right]^2 \left[6 - 4\left(\frac{V_0}{V}\right)^{2/3}\right]\right\}, \quad (13)$$

where E_0 is the electronic energy of AmO_2 at its equilibrium volume V_0, B_0 is the bulk modulus, and B_0' is the pressure derivative of the bulk modulus. The numerically fitted lattice constants, B_0, and B_0' are summarized in Table I. For comparison, the experimental values [42, 43] and HSE theoretical results [7] are also listed. One can see that the LDA and LDA+U results on the lattice constant a_0 are both smaller, while the GGA and GGA+U results are both larger than the experimental values. This fact reflects the overbinding effect of LDA and the underbinding effect of GGA on the chemical bonding strengths between different atoms. However, all the obtained lattice constants are not too far away from the experimental values. As for bulk modulus B_0, it displays strong dependence on the U values for both LDA+U and GGA+U approaches. As U increases from 0 to 4 eV, B_0 decreases monotonously by 12.9% and 21.9% for LDA+U and GGA+U calculations, respectively. Due to overbinding effect of LDA and underbinding effect of GGA, the LDA+U results of B_0 are always higher than the GGA+U ones. We have also calculated the bulk modulus B_0 from empirical formula based on the elastic constants (as shown in Table III), which turns out to be very close to the result by EOS fitting, indicating that our calculations are self-consistent. Moreover, through EOS fitting, we also systematically obtain the pressure derivative of bulk modulus by using different methods. The corresponding results are also listed in Table I.

Through electronic structure calculations, we find that without employing the +U method describing the strong electron correlation effect, AmO_2 is wrongly described to be metallic in its ground state. Figure 1 shows the projected density of states (PDOS) for AmO_2 obtained with different computational methods. Since spin-orbital coupling (SOC) effects might be important to electronic structure descriptions of actinide dioxides, here we consider SOC in all calculations. In the LDA/GGA calculational level, SOC makes americium $5f$ orbitals to split into the lower j=5/2 ($f_{5/2}$) and higher j=7/2 ($f_{7/2}$) orbitals, occupying below and above the Fermi energy respectively, as shown in Figs. 1(a) and 1(c). The obtained electronic states show metallic characters with considerable $f_{5/2}$ states distributing at the

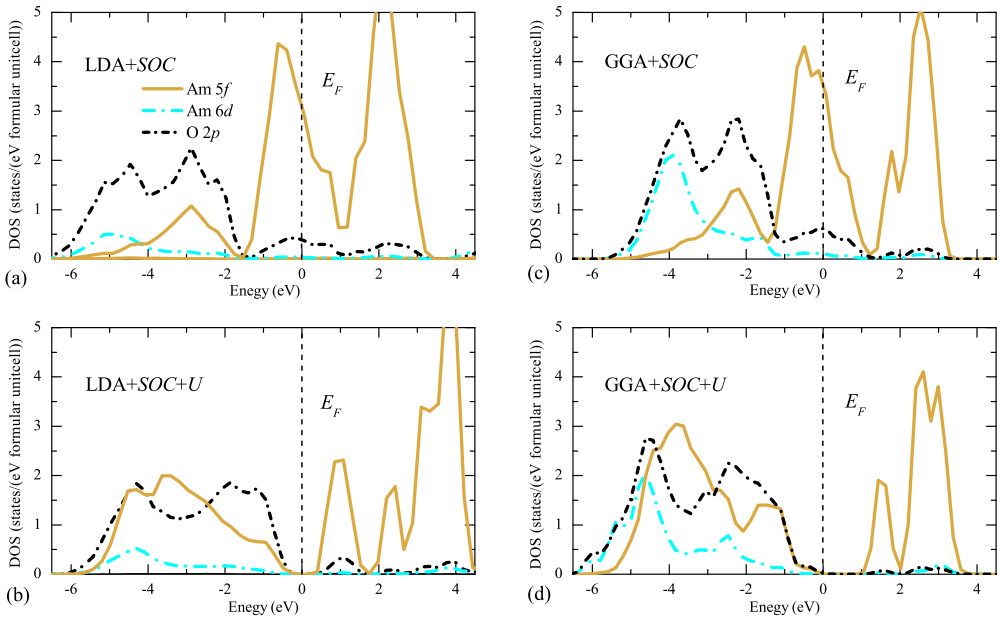

FIG. 1: (Color online). Electronic density of states for AmO_2 in its AFM state calculated by using the (a) LDA, (b) LDA+U, (c) GGA, and (d) GGA+U methods. The spin-orbit coupling is included in all calculations. The value for the U parameter is chosen to be 4 eV for all LDA+U and GGA+U calculations. The Fermi energy is set at zero.

Fermi energy. However, after turning on the U-parameter to describe the strong on-site electron correlation effects of americium $5f$ electrons, the $f_{5/2}$ state is further split into two separate sub-bands, distributing at the two sides of the Fermi energy. As shown in Figs. 1(b) and 1(d), an obvious energy band gap appears in LDA/GGA+U calculations. Within LDA and GGA+U calculations, the energy band gap of AmO_2 is found to be 0.7 and 1.0 eV respectively, as shown in Table I. As will be discussed below, the difference between the obtained energy band gaps might come from the different hybridization strengths of the americium $5f$ and $6d$ states in LDA/GGA+U calculations. The obtained insulating ground state of AmO_2 is in agreement with previous hybrid density functional result [7], where the energy band gap is found to be 1.6 eV. From the obtained PDOS distributions shown in Figs. 1(b) and 1(d), we can see that the americium $5f$ and $6d$ states hybridize below the Fermi energies, and this hybridization is stronger in GGA+U than in LDA+U calculations. The stronger hybridization moves the $5f$ states lower, and results in the fact that the band gap is larger in GGA+U calculations. The calculated local spin moment of each americium ion are 4.94 μ_B and 5.15 μ_B in the LDA+U and GGA+U calculations respectively, which

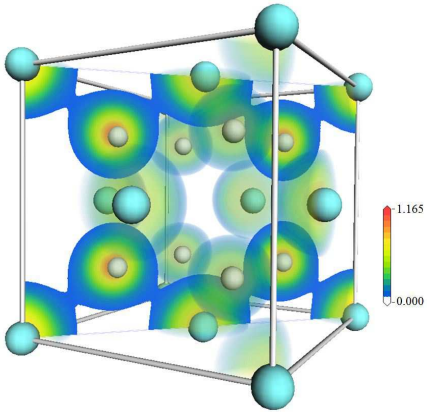

FIG. 2: (Color online). The cubic cell of AmO_2 with $Fm\bar{3}m$ space group, and a contour map depicting the charge density distribution inside the (110) plane. Large cyan and small white balls represent for americium and oxygen atoms respectively. The charge density distribution is calculated by using the GGA+U method with the U parameter of 4 eV.

are both similar to the 5.1 μ_B result obtained in hybrid density functional calculations [7].

To further understand the chemical bonding characters of AmO_2, we present in Fig. 2 the charge density distribution inside the (110) plane. Similar to what we have found in our previous studies on other actinide dioxides [11, 18], the charge density distribution around the Am and O ions are both spherical, with small deformations in the directions toward their nearest neighboring ions. This character is typical for mixed ionic/covalent chemical bondings in actinide dioxides [11]. By employing the Bader analysis [44, 45] which decomposes the charge density distribution in real space following topological methods, we further calculate the atomic charges for Am and O ions and present the results in Table II. Note that although we have included the core charge in charge density calculations, only the valence charge results are listed. Given that the valence electron numbers of Am and O atoms are 17 and 6, about 2.26 electrons transfer from each Am to O atoms. In our previous studies, we have also applied similar DFT+U calculations for UO_2, NpO_2, and PuO_2 [11, 18] and found that the charge transfer from each actinide to oxygen atoms is 2.56 for UO_2, 2.48 for NpO_2, and 2.40 for PuO_2. From the charge transfer results, we can see that with increasing the atomic number of the actinide elements, the chemical bondings between actinide and oxygen atoms show less ionic characters. In addition, the bonding lengths of the dioxides are also listed in Table II. Accompanying with the weakening of ionicity, the bonding lengths between actinide and oxygen atoms decrease with increasing the atomic

TABLE II: Calculated atomic charges according to Bader partitioning as well as the bonding lengths of different actinide dioxides.

Compound	$Q_B(A)$ (e)	Q_B(O) (e)	bonding length (Å)
AmO_2	14.74	7.13	2.27
PuO_2[a]	13.60	7.20	2.32
NpO_2[b]	12.52	7.24	2.34
UO_2[a]	11.44	7.28	2.36
ThO_2[c]	9.34	7.33	2.43

[a] Reference 11.

[b] Reference 18.

[c] Reference 46.

number of actinide elements.

B. Mechanical properties

Based on the Hooke's law, we systematically calculate the three independent elastic constants for AmO_2 within the GGA+U formalism. The results are listed in Table III together with our previous results on other actinide dioxide materials. At the value of U=4 eV, the calculated values of C_{11}, C_{12}, and C_{44} are 250.4, 87.0, and 55.3 GPa respectively. Mechanically, the phase of AmO_2 is stable due to the fact that its elastic constants satisfy the following mechanical stability criteria [37] of cubic structure:

$$C_{11} > 0,\ C_{44} > 0,\ C_{11} > |C_{12}|,\ (C_{11} + 2C_{12}) > 0. \tag{14}$$

Among the actinide dioxide series listed in Table III, the elastic constants of AmO_2 have the lowest values. Based on the elastic constants, we can further calculate the bulk and shear moduli from the Voigt-Reuss-Hill (VRH) approximations. Firstly, the Voigt and Reuss limits on the bulk ($B_{\rm V}$ and $B_{\rm R}$) and shear moduli ($G_{\rm V}$ and $G_{\rm R}$) are calculated following the expressions in Refs. 47, 48, then the bulk and shear moduli can be approximately evaluated by $B = \frac{1}{2}(B_{\rm V} + B_{\rm R})$ and $G = \frac{1}{2}(G_{\rm V} + G_{\rm R})$ [49]. In addition, the Young′s modulus

E and Poisson′s ratio ν can also be evaluated from the elastic constants by $E = \frac{9BG}{3B+G}$ and $\nu = \frac{3B-2G}{2(3B+G)}$, respectively. Our results for mechanical properties of AmO_2 by using the GGA+U method are collected in Table III. The value of 141.5 GPa for bulk modulus B is in agreement with the EOS-fitting result of 140.1 GPa. Besides, in comparison with other actinide dioxides included in Table III, the value of B for AmO_2 is much lower. This means that when external pressures are applied on these actinide dioxides, AmO_2 will be the easiest to get cracked. For the shear modulus, we can see that PuO_2 and AmO_2 have relatively smaller values than UO_2, NpO_2, and ThO_2. This result comes from the fact that the oxygen $2p$ and actinide $5f$ electronic states have more overlaps in PuO_2 and AmO_2, and subsequently the chemical bondings between oxygen and actinide atoms show more covalent characters in PuO_2 and AmO_2. Considering that the values of B and G represent for the ability to resist external pressures and shearing forces respectively, Pugh *et al.* suggested that their quotient B/G can be used to scale the ductility or brittleness of a solid [50]. A high value of B/G means that the material has more ductility than brittleness, and a critic value of 1.75 is suggested to distinguish ductile or brittle materials. Our calculated value of 2.19 for B/G means that AmO_2 is a ductile material. At last, our calculated Young's modulus and Poisson's ratio for AmO_2 are 168.4 GPa and 0.302 respectively, both of which are among the typical values of insulating oxide materials.

The Debye temperature (Θ) of a solid can be determined following the Debye theory, which describes atomic vibrations to be elastic waves, and subsequently Θ is related to the sound velocity of a material [51]. Specifically,

$$\Theta = \frac{h}{k_B}\left(\frac{3n}{4\pi\Omega}\right)^{1/3} v_m, \tag{15}$$

where h and k_B are Planck and Boltzmann constants, respectively, n is the number of atoms in one unit cell, Ω is the volume per unit cell, and v_m is the averaged sound velocity. Approximately, the averaged sound velocity can be calculated by

$$v_m = \left[\frac{1}{3}\left(\frac{2}{v_t^3} + \frac{1}{v_l^3}\right)\right]^{-1/3}, \tag{16}$$

where $v_t = \sqrt{G/\rho}$ (ρ is the density of a material) and $v_l = \sqrt{(3B+4G)/3\rho}$ are the transverse and longitudinal elastic wave velocities, B and G are the bulk and shear moduli. Our calculated sound velocities and Debye temperature of AmO_2 are also listed in Table III. For comparison, our previous results for other actinide dioxides are also included. We

TABLE III: Calculated elastic constants, various moduli, and Poisson′s ratio ν for AmO_2. For comparisons, previous experimental values and other theoretical results are also listed.

	C_{11} (GPa)	C_{12} (GPa)	C_{44} (GPa)	B (GPa)	G (GPa)	E (GPa)	ν	v_t (m/s)	v_l (m/s)	v_m (m/s)	Θ (K)
AmO_2	250.4	87.0	55.3	141.5	64.7	168.4	0.302	2416.6	4534.1	2699.8	335.7
PuO_2[a]	256.5	167.9	59.2	197	52.7	145.2	0.377	2477.6	5206.3	2787.0	354.5
NpO_2[b]	363.6	118.8	57.4	200	78.1	207.5	0.327	2835.0	5566.5	3176.8	401.2
UO_2[a]	389.3	138.9	71.3	222.4	89.5	236.7	0.323	2841.8	5552.7	3183.4	398.1
ThO_2[c]	349.5	111.4	70.6	191	87.1	226.8	0.302	2969.1	5575.5	3317.3	402.6

[a] Reference 11.

[b] Reference 18.

[c] Reference 46.

can see from Table III that the v_t and v_l values of AmO_2 are lower than those of PuO_2, UO_2, NpO_2, and ThO_2. Since the sound velocity of a compound is always related to its lattice thermal conductivity, this result reflects that AmO_2 has smaller thermal transport properties. Because the Debye temperature is proportional to v_m, AmO_2 among the listed actinide dioxides possesses the lowest Debye temperature.

C. Theoretical tensile strength

Based on the obtained atomic structure of AmO_2, we further study its theoretical tensile strength. The ideal strength of materials is the stress that is required to force deformation or fracture at the elastic instability. Although the strength of a real crystal can be changed by the existing cracks, dislocations, grain boundaries, and other microstructural features, its theoretical value can never be raised, i.e., the theoretical strength sets an upper bound on the attainable stress. Here, we employ a first-principles computational tensile test (FPCTT) [52] to calculate the stress-strain relationship and obtain the ideal tensile strength by deforming the AmO_2 crystals to failure. The anisotropy of the tensile strength is tested by pulling the initial fluorite structure along the low-index [001], [110], and [111] directions. As shown in

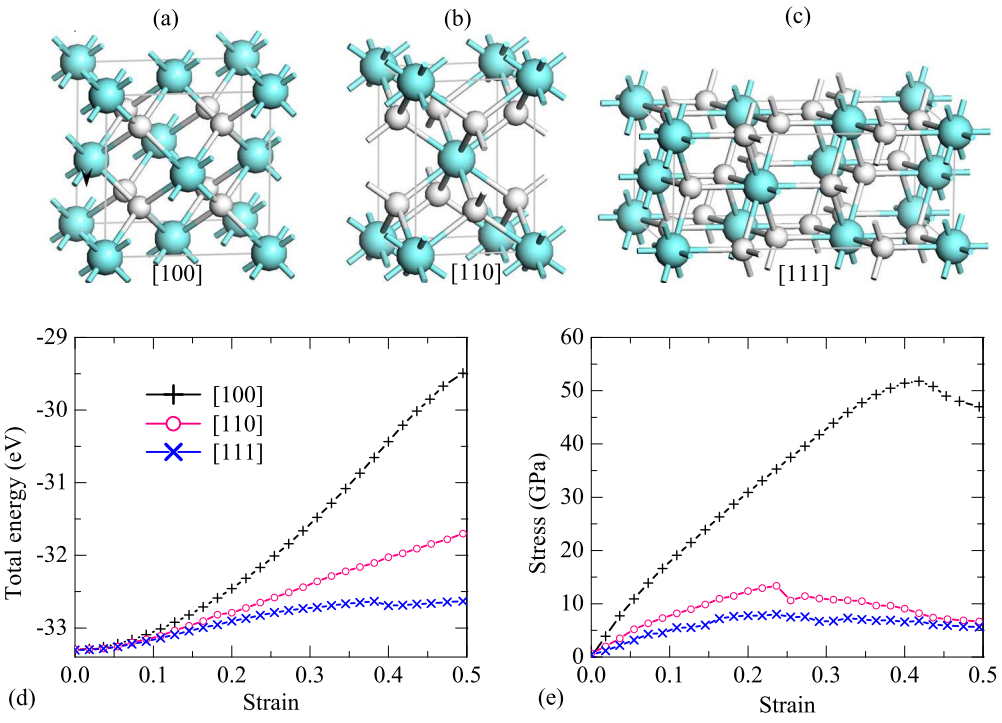

FIG. 3: (Color online). Schematic illustration of structure models for applying tensions along the [100] (a), [110] (b), and [111] (c) directions. (d) and (e) Total energies per formula unit and stresses for AmO_2 being pulled along the [100], [110], and [111] directions.

Figs. 3(a)-3(c), three geometric structures are constructed to investigate the tensile strengths in the three high-symmetry crystallographic directions: Fig. 3(a) shows a general fluorite structure of AmO_2 with four Am and eight O atoms; Fig. 3(b) a body-centered tetragonal unit cell with two Am and four O atoms; and Fig. 3(c) an orthorhombic unit cell with six Am and twelve O atoms. The tensile stress is calculated according to the Nielsen-Martin scheme [53] $\sigma_{\alpha\beta} = \frac{1}{\Omega}\frac{\partial E_{total}}{\partial \varepsilon_{\alpha\beta}}$, where $\varepsilon_{\alpha\beta}$ is the strain tensor (α, β=1, 2, 3) and Ω is the volume at the given tensile strain. Tensile process along the [001], [110], and [111] directions is implemented by increasing the lattice constants along these three orientations step by step. At each step, the structure is fully relaxed until all other five stress components vanished except that in the tensile direction.

The calculated total energies and stresses as functions of uniaxial tensile strains for AmO_2 along the [100], [110], and [111] directions are shown in Figs. 3(d) and 3(e). One can see that with increasing the tensile strains along all the three directions, the energies increase with inflexions. By differentiating the energy-strain curves, we find the inflexion points

TABLE IV: Calculated strain energy (E_{strain}) and stress maxima at the critic points in the tensile processes.

Direction	Strain	E_{strain} (eV/atom)	Stress (GPa)
[100]	0.42	2.87	51.8
[110]	0.24	0.64	13.4
[111]	0.18	0.35	4.6

along the [100], [110], and [111] directions to be the strain values of 0.42, 0.24, and 0.18 respectively. At these strain values, the corresponding energy increases are 2.87, 0.64, and 0.35 eV per atom in AmO_2, and the corresponding stress maxima are 51.8, 13.4, and 7.6 GPa respectively, as shown in Table IV. Since the stress-strain curves change from upward into downward at these inflexion points, the stress maxima values are regarded as the theoretical tensile strengths. Clearly along the three low-index directions, the [100] direction has the largest, while the [111] direction has the smallest tensile strength. This result is similar to what we have found in another actinide dioxide PuO_2 [11]. We can also understand this result from chemical bonding analysis. Along the [100] direction, there are eight Am-O bonds per formula unit for fluorite AmO_2, and the angle of all eight bonds with respect to the pulling direction is 45°. In comparison, along the [110] and [111] directions only four and two Am-O bonds make an angle of 45° with the pulling direction. The other four bonds along the [110] direction are vertical to the pulling direction, while the other six bonds make an angle of about 70.5° with the pulling direction. It is evident that the bonds vertical to the pulling direction have no contributions to the tensile strength, and the bonds parallel to the pulling direction are easy to fracture under tensile deformation. Therefore, the tensile strength along the [100] direction is stronger than that along other two directions. Along all the three direction, no structural transition has been observed under external strains in our present study. Besides, we note that the stress in [110] direction experiences an abrupt decrease process after strain up to 0.24. This is due to the fact that the corresponding four Am-O bonds making an angle of 45° with the pulling direction have been pulled to fracture under that strain. In comparison with PuO_2 [11], we can see that the theoretical tensile strengths of AmO_2 are much smaller along all the three low-index directions, indicating that

AmO_2 is easier to get deformed during tensile processes.

D. Phonon dispersion curves and thermodynamic properties

To our knowledge, no experimental or theoretical phonon frequency results have been published for AmO_2. Here we carry out the first theoretical try in obtaining its phonon dispersion curves, as well as thermodynamic properties. The density functional perturbation theory (DFPT) and a 2×2×2 supercell containing 96 atoms is adopted to calculate the force constants of AmO_2. Since our previously obtained phonon dispersion curves result by using the same methods for PuO_2 accords moderately well with subsequent experimental measurements, we are confident that our present results for AmO_2 can be effective to certain degrees. The Born effective charges are firstly calculated to reveal the dielectric properties of AmO_2, and to modify the LO-TO (longitudinal optical and transverse optical branches of phonon) splitting effects. For fluorite AmO_2, the effective charge tensors for both Am and O are isotropic because of their position symmetry. After calculation, the Born effective charges of Am and O ions are found to be $Z^{\star}_{\mathrm{Am}} = 4.51$ and $Z^{\star}_{\mathrm{O}} = -2.26$, respectively, within GGA+U formalism with the choice of U=4.0 eV. We present in the left panel of Fig. 4 (solid lines) our calculated phonon dispersion curves for AmO_2. In the fluorite primitive cell, there are three atoms (one Am and two O atoms). Therefore, nine branches of phonon dispersion curves exist. One can see that the LO-TO splitting at Γ point becomes evident by the inclusion of polarization effects. In addition, due to the fact that americium atom is heavier than oxygen atom, the vibration frequency of americium atom is lower than that of oxygen atom. As a consequence, the phonon density of states for AmO_2 can be viewed as two parts, as shown in the right panel of Fig. 4. One is the part lower than 4.0 THz where the main contribution comes from the americium sublattice while the other part higher than 4.0 THz are dominated by the dynamics of the light oxygen atoms.

To investigate the effects of strains on the phonon dispersion, we also calculate the phonon spectrum for AmO_2 that is stretched with an isotropic strain of 0.03, and show the results in Fig. 4 with dashed lines. Clearly after being expanded, both the acoustic and optical branches of phonon experience frequency shift downward, indicating the weakening of atomic interactions.

The thermodynamic properties of a material are connected to its phonon dispersion

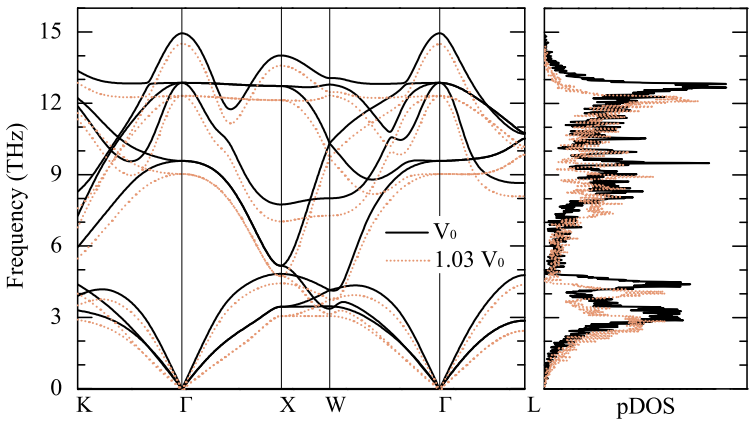

FIG. 4: (Color online). Phonon dispersion curves along the high symmetry lines of the Brillouin Zone (left panel) and phonon density of states (right panel) for AmO_2 at the equilibrium and expanded volumes. Solid and dashed lines represent for the results at the equilibrium and expanded volumes respectively. The expansion ratio is 0.03 for the expanded lattice calculations.

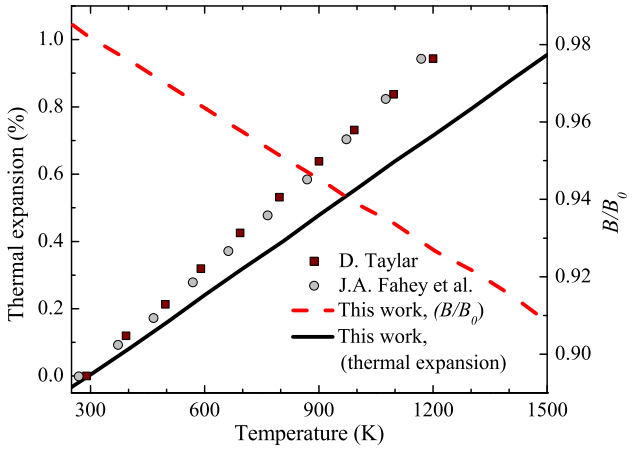

FIG. 5: (Color online). Temperature dependence of our calculated linear thermal expansion (solid line) and bulk modulus ratio (dashed line), and the experimentally measured lattice expansion results for AmO_2.

curves. By systematically calculating the Helmholtz free energies at different lattice constants and different temperatures, we can determine the lowest-energy lattice constant for AmO_2 at different temperatures. As expected, the lattice constant enlarges as temperature increases. And the obtained lattice expansion curve for AmO_2 is shown in Fig. 5, together with the experimental results by Taylar *et al.* [54] and Fahey *et al.* [55]. Similar linear relationships can be found in our theoretical and previous experimental results. The small

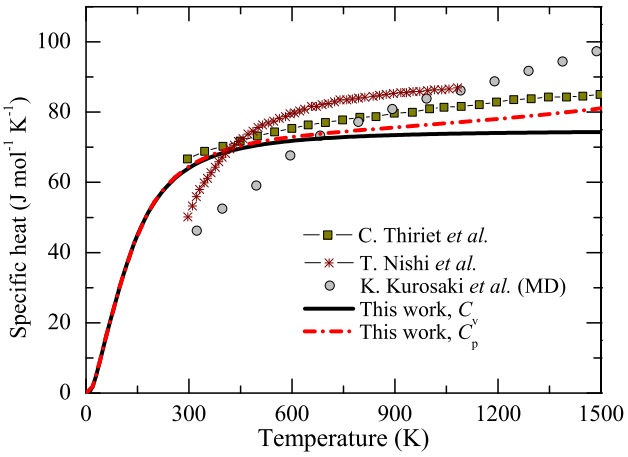

FIG. 6: (Color online). Calculated heat capacities of AmO_2 at constant volume (C_v) and constant pressure (C_p), and corresponding experimental results as well as other theoretical results.

difference on the increasing ratios comes from the fact that we only consider harmonic vibrations during calculations of the phonon dispersion curves and the Helmholtz free energy. By fitting the Brich-Murnaghan EOS for AmO_2 at different temperatures for AmO_2, we also obtain the temperature dependence of its bulk modulus B. And our result of B/B_0 as a function of temperature T is also shown in Fig. 5. One can see that as temperature increases, the bulk modulus decreases, indicating that AmO_2 is easier to get cracked at higher temperatures.

Within QHA the heat capacity at constant volumes can be calculated following Eqs. (5) and (6). Besides, the heat capacity at constant pressure C_p can be further evaluated by using the relationship

$$C_p - C_v = \alpha_v^2(T)B(T)V(T)T.$$

We then calculate the heat capacities for AmO_2, and show the results in Fig. 6. For comparison, the experimental data by Thiriet *et al.* [56] and Nishi *et al.* [43] are also shown in Fig. 6. We can see that with increasing the temperature, the value of C_p increases continuously, while the value of C_v approaches to a constant of $3R$ (R is the gas constant). As clearly shown, our theoretical result for C_p is in good agreement with the experimental measurements by Thiriet *et al.* [56] at the temperature range from 300 to 500 K. As temperature further increases, the discrepancy between our result and the experimental values [43, 56] become larger. We conclude that the disagreement of C_p between theory and experiments in the high temperature range mainly originates from the QHA we used. Due to anharmonic

effects, our obtained lattice expansion curve is lower than experimental results, as shown in Fig. 5. The underestimation on the lattice expansion of AmO_2 finally results in the discrepancies between our calculated C_p values and corresponding experimental results through the above relationship between C_p and C_v.

E. Grüneisen parameters and thermal conductivity

Based on the calculated phonon dispersion curves of AmO_2 at both the equilibrium and expanded lattice volumes, we can further calculate the Grüneisen parameters for each vibration mode of AmO_2. Our obtained Grüneisen parameters at different k points are shown in Fig. 7. Due to the fact that after lattice expansion, atomic interactions are weakened and phonon frequencies are lowered, the Grüneisen parameters are positive for almost all phonon branches. The only exception lies around the W point, where the Grüneisen parameter for the second acoustic branch of phonon has a small negative value. This result comes from the coupling behavior of the two lowest-frequency acoustic phonon branches at the W point. After lattice expansion, the coupling disappears and the dispersion curves of these two branches separate with each other, causing that the frequency of the higher branch moves upward. As a result, the Grüneisen parameters for this phonon branch have small negative values around the W point.

We have explained above that the Umklapp scattering $\frac{1}{\tau_U}$ is proportional to γ^2, thus, the Grüneisen parameter provide an estimate of the strength of anharmonicity in a compound. One can see from Fig. 7 that the two transverse acoustic branches of phonons have the largest Grüneisen parameters, indicating that these two branches are most anharmonic and interact with the longitudinal acoustic mode strongly. In order to describe quantitatively the anharmonic effects, we further calculate the average Grüneisen parameter ($\bar{\gamma}$) for the three acoustic vibration modes by using the similar method proposed in Ref. [38]: $\bar{\gamma} = \sqrt{\langle \gamma_i^2 \rangle}$. For AmO_2, the values of $\bar{\gamma}_{TA}$, $\bar{\gamma}_{TA'}$, $\bar{\gamma}_{LA}$ are 2.75, 2.48, and 2.16, respectively. And the average $\bar{\gamma}$ of the three acoustic modes is then calculated to be 2.46. These transverse modes play an important role in lattice thermal resistance. Furthermore, since the velocity of transverse modes is much lower than the longitudinal one, the lattice thermal conductivity is dominated by the lower-velocity transverse modes.

The acoustic Debye temperature closely related to the lattice thermal conductivity of a

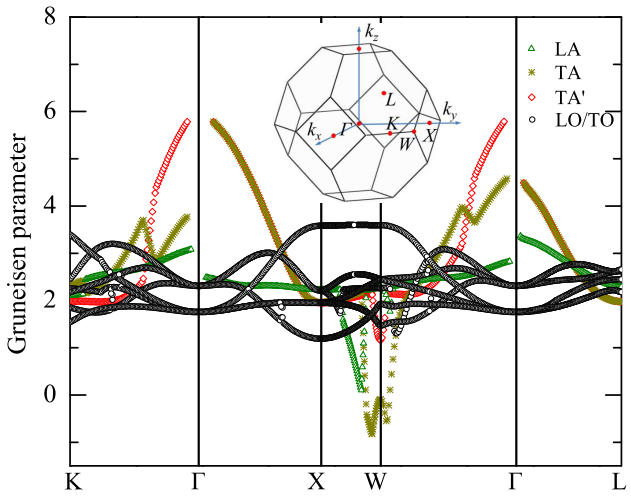

FIG. 7: (Color online). Calculated Grüneisen parameters for AmO_2. Blue, red, and olive symbols represent for the results corresponding to the two transverse acoustic (TA and TA′) and one longitudinal acoustic (LA) branches of phonon respectively. The inset depicts the first Brillouin zone.

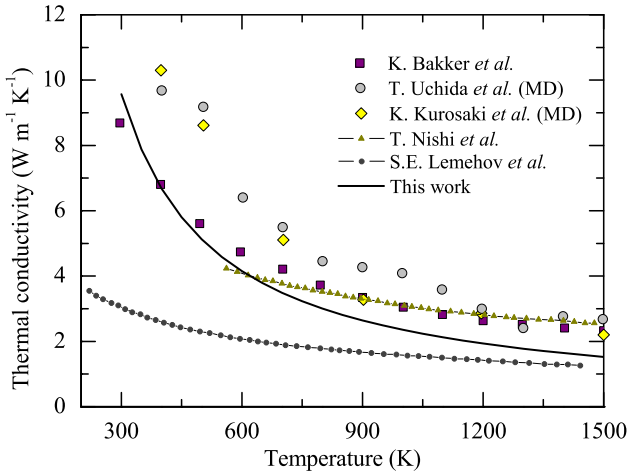

FIG. 8: (Color online). Calculated lattice thermal conductivity for AmO_2 at different temperatures, and corresponding experimental as well as other theoretical results.

material can be approximately calculated by using the relationship [57, 58]

$$\Theta_a = \Theta n^{-1/3},$$

where Θ and n are the Debye temperature and number of atoms in the unit cell, respectively. For AmO_2, Θ_a is calculated to be 233.0 K. Based on the relationship in Eq. (9), and the above obtained quantities, we calculate the lattice thermal conductivity for AmO_2 and show

the results from the temperature of 300 K to 1500 K in Fig. 8. For comparison, previous experimental results by Bakker *et al.* [59] and Nishi *et al.* [43], as well as theoretical results by Uchida *et al.* [60], Kurosaki *et al.* [61], and Lemehov *et al.* [62] are also shown in Fig. 8. Clearly, in the temperature range from 300 to 700 K, our theoretical results accord well with the experimental measurements. At the higher temperature range of above 700 K, our calculated thermal conductivity are a little smaller than the corresponding experimental results. This disagreement might come from two different factors. Firstly, the electronic thermal conductivity which occupies larger ratios at higher temperatures is not considered here because of limitations of our computational methods. Secondly, the Debye-Callaway model we used does not take into account the optical branches of phonons, some of which have appreciable group velocities and are able to contribute to thermal conductivity. Overall, the coarse agreement between our theoretical results on thermal conductivity with the experimental ones is fortuitous.

IV. CONCLUSIONS

In summary, a thorough DFT+U study has been performed to investigate the electronic, mechanical, and thermodynamical properties of AmO_2. It is found that the chemical bonding between the americium and oxygen atoms show mixed ionic and covalent characters. The valence band maximum and conduction band minimum are contributed by $2p$-$5f$ hybridized and $5f$ electronic states respectively. In comparison with PuO_2, the bonding length and charge transfer in AmO_2 are both slightly smaller, indicating stronger covalent and weaker ionic interactions in the latter than than in the former. Through calculations of the elastic constants and various moduli, we have predicted that compared to PuO_2, AmO_2 is more stable against shear forces, but less stable against pressures. The stress-strain relationship of AmO_2 has also been examined along the three low-index directions by FPCTT calculations. Our results show that the [100] and [111] directions are the strongest and weakest tensile directions, respectively. In comparison with PuO_2, the theoretical tensile strengths of AmO_2 are smaller. At the thermodynamic aspects, the phonon dispersion of AmO_2 has been calculated at different lattice volumes, with the LO-TO splitting effect being modified through Born effective charges. Subsequently, we have systematically obtained the heat capacities and lattice expansion curve, both of which accord well with the experiments. Fi-

nally, by differentiating the phonon dispersion curves at different lattice constants, we have further calculated the Grüneisen parameters of AmO_2 and determined its lattice thermal conductance at different temperatures, which show the overall agreement with attainable experimental measurements.

Acknowledgments

This work was supported by NSFC under Grant No. 51071032 and 11104170, and by Foundations for Development of Science and Technology of China Academy of Engineering Physics under Grants Nos. 2011A0301016 and 2011B0301060.

[1] S. Y. Savrasov, G. Kotliar, and E. Abrahams, Nature **410**, 793 (2001).

[2] R. C. Albers, Nature **410**, 759 (2001).

[3] S. S. Hecker, Metall. Mater. Trans. A **35**, 2207 (2004).

[4] K. T. Moore, G. van der Laan, R. G. Haire, M. A. Wall, and A. J. Schwartz, Phys. Rev. B **73**, 033109 (2006).

[5] I. D. Prodan, G. E. Scuseria, J. A. Sordo, K. N. Kudin, and R. L. Martin, J. Chem. Phys. **123**, 014703 (2005).

[6] I. D. Prodan, G. E. Scuseria, and R. L. Martin. Phys. Rev. B **73**, 045104 (2006).

[7] I. D. Prodan, G. E. Scuseria, and R. L. Martin. Phys. Rev. B **76**, 033101 (2007).

[8] B. Sun, P. Zhang, and X. G. Zhao, J. Chem. Phys. **128**, 084705 (2008).

[9] D. A. Andersson, J. Lezama, B. P. Uberuaga, C. Deo, and S. D. Conradson, Phys. Rev. B **79**, 024110 (2009).

[10] G. Jomard, B. Amadon, F. Bottin, and M. Torrent, Phys. Rev. B **78**, 075125 (2008).

[11] P. Zhang, B. T. Wang, and X. G. Zhao, Phys. Rev. B **82**, 144110 (2010).

[12] H. Nakamura, M. Machida, and M. Kato, Phys. Rev. B **82**, 155131 (2010).

[13] L. Petit, A. Svane, Z. Szotek, W. M. Temmerman, and G. M. Stocks, Phys. Rev. B **81**, 045108 (2010).

[14] C. Duriez, J. P. Alessandri, T. Gervais, Y. Philipponneau, J. Nucl. Mater. **277**, 143 (2000).

[15] M. Inoue, J. Nucl. Mater. **282**, 186 (2000).

[16] T. Arima, S. Yamasaki, Y. Inagaki, K. Idemitsu, J. Alloys Comp. **415**, 43 (2006).

[17] P. Martin, S. Grandjean, C. Valot, G. Carlot, M. Ripert, P. Blanc, C. Hennig, J. Alloys Comp. **444-445**, 410 (2007).

[18] B. T. Wang, H. L. Shi, W. D. Li, and P. Zhang, Phys. Rev. B **81**, 045119 (2010).

[19] G. M. Kalvius, S. L. Ruby, B. D. Dunlap, G. K. Shenoy, D. Cohen, and M. B. Brodsky, Phys. Lett. **29B**, 489 (1969).

[20] D. G. Karraker, J. Chem. Phys. **63**, 3174 (1975).

[21] S. B. Wilkins, R. Caciuffo, C. Detlefs, J. Rebizant, E. Colineau, F. Wastin, and G. H. Lander, Phys. Rev. B **73**, 060406 (2006).

[22] P. Santini, S. Carretta, G. Amoretti, R. Caciuffo, N. Magnani, and G. H. Lander, Rev. Mod. Phys. **81**, 807 (2009).

[23] M. Sanati, R. C. Albers, T. Lookman, and A. Saxena, Phys. Rev. B **84**, 014116 (2011).

[24] L. Petit, A. Svane, Z. Szotek, and W. M. Temmerman, Science **301**, 498 (2003).

[25] Q. Yin and S. Y. Savrasov, Phys. Rev. Lett. **100**, 225504 (2008).

[26] H. L. Shi, M. F. Chu, and P. Zhang, J. Nucl. Mater. **400**, 151 (2010).

[27] J. Schoenes, J. Appl. Phys. **49**, 1463 (1978).

[28] F. D. Bruycker, K. Boboridis, D. Manara, P. Pöml, M. Rini, and R. J. M. Konings, Materials Today **13**, 52 (2010)

[29] M. E. Manley, J. R. Jeffries, A. H. Said, C. A. Marianetti, H. Cynn, B. M. Leu, and M. A. Wall, Phys. Rev. B **85**, 132301 (2012).

[30] G. Kresse and J. Furthmuller, Phys. Rev. B **54**, 11169 (1996) and references therein.

[31] P. E. Blöchl, Phys. Rev. B **50**, 17953 (1994).

[32] J. P. Perdew, K. Burke, M. Ernzerhof, Phys. Rev. Lett. **77**, 3865 (1996).

[33] H. J. Monkhorst and J. D. Pack, Phys. Rev. B **13**, 5188 (1976).

[34] S. L. Dudarev, D. N. Manh, and A. P. Sutton, Philos. Mag. B **75**, 613 (1997).

[35] S. L. Dudarev, G. A. Botton, S. Y. Savrasov, C. J. Humphreys, and A. P. Sutton, Phys. Rev. B **57**, 1505 (1998).

[36] S. L. Dudarev, M. R. Castell, G. A. Botton, S. Y. Savrasov, C. Muggelberg, G. A. D. Briggs, A. P. Sutton, and D. T. Goddard, Micron **31**, 363 (2000).

[37] J. F. Nye, Physical Properties of Crystals (Oxford University Press, Oxford, 1985).

[38] D. T. Morelli, J. P. Heremans, and G. A. Slack, Phys. Rev. B **66**, 195304 (2002).

[39] M. A. Palmer, K. Bartkowski, E. Gmelin, M. Cardona, A. P. Zhernov, A. V. Inyushkin, A. Taldenkov, V. I. Ozhogin, K. M. Itoh, and E. E. Haller, Phys. Rev. B **56**, 9431 (1997).

[40] J. Callaway, Phys. Rev. **113**, 1046 (1959).

[41] F. Brich, Phys. Rev. **71**, 809 (1947).

[42] D. H. Templeton and C. H. Dauben, J. Am. Chem. Soc. **75** 4560 (1953).

[43] T. Nishi, M. Takano, A. Itoh, M. Akabori, Y. Arai, K. Minato, and M. Numata, J. Nucl. Mater. **373**, 295 (2008).

[44] R. F. W. Bader, *Atoms in Molecules: A Quantum Theory* (Oxford University Press, New York, 1990).

[45] W. Tang, E. Sanville, and G. Henkelman, J. Phys.: Condens. Matter **21**, 084204 (2009).

[46] B. T. Wang, H. L. Shi, W. D. Li, and P. Zhang, J. Nucl. Mater. **399**, 181 (2010).

[47] W. Voigt, Lehrburch der Kristallphysik, Teubner, Leipzig, (1928).

[48] A. Reuss, Z. Angew. Math. Mech. **9** 49 (1929).

[49] R. Hill, Proc. Phys. Soc., London, Sect. A **65**, 349 (1952).

[50] S. F. Pugh, Philos. Mag. **45**, 823 (1954).

[51] A. A. Blanco, E. Francisco, and V. Luana, Comput. Phys. Commun. **158**, 57 (2004).

[52] Y. Zhang, G. H. Lu, S. H. Deng, T. M. Wang, H. B. Xu, M. Kohyama, and R. Yamamoto, Phys. Rev. B **75**, 174101 (2007).

[53] O. H. Nielsen and R. M. Martin, Phys. Rev. B **32**, 3780 (1985).

[54] D. Taylar, J. Thermal Expansion Data **84**, 181 (1985).

[55] J. A. Fahey, R. P. Turcotte, and T. D. Chikalla, Inorg. Nucl. Chem. Lett. **10**, 459 (1974).

[56] C. Thiriet and R. J. M. Konings, J. Nucl. Mater. **320**, 292 (2003).

[57] O. L. Anderson, J. Phys. Chem. Solids **12**, 41 (1959).

[58] G. A. Slack, Solid State Phys. **34**, 1 (1979).

[59] K. Bakker and R. J. M. Konings, J. Nucl. Mater. **254**, 129 (1998).

[60] T. Uchida, T. Arima, K. Idemitsu, and Y. Inagaki, Comp. Mater. Sci. **45**, 229 (2009).

[61] K. Kurosaki, M. Imamura, I. Sato, T. Namekawa, M. Uno, and S. Yamanaka, J. Nucl. Sci. Technol. **41**, 827 (2004).

[62] S. E. Lemehov, V. Sobolev, and P. V. Uffelen, J. Nucl. Mater. **320**, 66 (2003).